RSC Advances

ROYAL SOCIETY OF CHEMISTRY

www.rsc.org/advances

Preparation of RGO wrapped Magnetite Nanocomposites and its Energy Storage Properties

A. Shahul Hameed,[a] M. V. Reddy,[bc] B. V. R. Chowdari[b] and Jagadese J. Vittal[a]

Porous rGO/Fe_3O_4 nanocomposites have been prepared in this study by a simple precipitation reaction followed by freeze drying. When the sample was dried at 80 ºC, spinel phase of Fe_3O_4 wrapped by reduced graphene oxide sheets was obtained without any detectable impurities. It exhibits a high surface area of 30 m^2 g^{-1}. The rGO/Fe_3O_4 composites were also annealed at different conditions such as 600 ºC in Ar, 700 ºC in Ar and Ar-H_2 to understand the effect of annealing temperature on the electrochemical properties. The rGO content in the samples were found to be ~3-4 % in all the composites from CHNS analysis. Electrochemical properties of the different composites were investigated by cyclic voltammetry, galvanostatic cycling and EIS studies. The composite prepared at 80 ºC exhibits very high capacity of 1254 mAh g^{-1} for the first charge cycle. However, the capacity faded to 1046 mAh g^{-1} at the end of 40 cycles. Though the high temperature annealed samples show slightly decreased capacity, they show excellent capacity retention with good rate capability. The rGO/Fe_3O_4 composite obtained at 700 ºC in Ar-H_2 exhibits high reversible capacity of 480 mAh g^{-1} at a high current density of 3000 mA g^{-1}.

Introduction

In the recent years, various oxides containing iron such as Fe_2O_3,[1-4] Fe_3O_4,[5-8] MFe_2O_4 (M = Ni, Co, Mn, Zn),[9-14] etc., have attracted huge interest as anode materials for Li-ion batteries as a replacement for the commercial graphite. The lithium storage happens in these oxides via conversion (redox) mechanism whereby the oxides reversibly react with lithium forming Li_2O along with metal nanoparticles. These oxides have great advantages of high reversible capacities, environmental benignity, low cost, abundance and slightly lower hysteresis compared to other metal oxides.[2, 15] However, their commercialization has been hindered by poor lithium cycling, high operating potentials and large polarization due to poor lithiation/de-lithiation kinetics which need to be addressed for utilization of these oxides as commercial anodes.

The magnetite phase (Fe_3O_4) is one of the attractive anodes and exhibits a normal spinel structure in which the divalent and trivalent cations occupy the tetrahedral and octahedral sites respectively. It undergoes reversible lithium storage via a conversion reaction with reversible formation of Fe nanoparticles in Li_2O matrix. It has a theoretical capacity of 926 mAh g^{-1}, assuming 8 moles of Li storage per mole of Fe_3O_4.

Lithium storage properties of iron oxide was reported to improve with size reduction to nanoparticles, owing to good Li transport as well as they ease the strain created by conversion reaction.[16] This improved electrochemical properties of the nanoparticles has motivated the synthesis of Fe_3O_4 in nanoscale by various routes like solvothermal,[17, 18] hydrothermal,[19, 20] carbothermal reduction,[21] sol gel,[22] electrospinning,[23] etc., for application in LIBs. In addition, different strategies like carbon coating,[24-26] compositing with CNT[27, 28] and graphene[29-31] have also been employed for the improvement of electronic conductivity of the material.

In this study, rGO wrapped magnetite nanoparticles were prepared by a simple precipitation method. Precipitation of GO/$FeSO_4$ solution by addition of NH_4OH followed by freeze drying of the colloidal mixture resulted in the formation of rGO/Fe_3O_4 nanocomposites. The effect of annealing temperature on the electrochemical investigation of these composites has affirmed stable and very high reversible capacity of the composites with good rate capability.

Experimental section

All the chemicals and solvents used in this study are commercially available and used without further purification.

Synthesis of Graphene oxide

Graphene oxide (GO) was prepared according to a previous literature.[32, 33] Graphite powder (2 g) was added carefully to an 80 °C mixture of conc. H_2SO_4 (3 mL), $K_2S_2O_8$ (1 g), and P_2O_5 (1 g), followed by stirring for few minutes till the mixture turned dark blue. Then it was allowed to cool to room temperature over a period of 8 hours. Later, it was carefully diluted with 1 L of distilled water which resulted in partial oxidation of graphite. It was filtered and washed with distilled water until the pH of the filtrate ~7. The powder was then dried overnight in air at room temperature.

The partially oxidized graphite powder (2 g) was slowly added to 50 mL of cold (0 ºC) conc. H_2SO_4 and 6 g of $KMnO_4$ was added in small amounts with continuous stirring so that the temperature of the mixture was never allowed to reach 20 ºC. After complete addition of $KMnO_4$, the temperature of the mixture was increased to 35 °C and stirred for another 2 h. Then, 200 mL of distilled water was added carefully. After 15 min, the reaction was terminated by addition of ~1 L of distilled water and 5 mL of 35 % H_2O_2 when the colour of the mixture changed to bright yellow. The mixture was filtered and washed with 1:10 HCl solution (500 mL) to remove the residual metal ions. The

resulting product was washed and suspended in distilled water to prepare 0.1 % (w/v) solution. To prepare graphene oxide (GO), the graphite oxide dispersion was exfoliated by sonication on an ultrasonic bath for 30 min. The resulting GO solution was yellowish brown in colour and was stable for a period of few months

Synthesis of rGO/Fe$_3$O$_4$

The rGO/Fe$_3$O$_4$ nanocomposites were prepared by a simple precipitation method coupled with freeze drying. In a typical synthesis, ~2.8 g (10 mmol) of FeSO$_4$·7H$_2$O was dissolved in ~200 mL of deionized water and ~50 mL of graphene oxide solution (0.1 wt %) was added and stirred for 12 h to obtain a homogeneous brown solution. During this step, partial oxidation of ferrous to ferric state occurs. Later, ammonium hydroxide was added drop-wise with continuous stirring until the pH of the mixture became neutral, resulting in the formation of a black colloidal solution which was then subjected to freeze drying for 12 h obtain porous powder. Freeze drying helps to prevent the aggregation of particles in comparison to normal drying. To prepare the rGO/magnetite nanocomposites, the obtained porous powder was heated at different conditions namely, (a) 80 °C in air, (b) 600 °C in Ar, (c) 700 °C in Ar and (d) 700 °C in Ar-H$_2$. The as-prepared rGO/Fe$_3$O$_4$ composites were black in colour. CHNS analysis revealed the percentage of rGO in the samples obtained at 80 and 600 °C to be ~4 % while the samples annealed at 700 °C has only ~3% rGO.

Structural and Electrochemical Characterization

The rGO/Fe$_3$O$_4$ nanocomposites prepared in this study were characterized by powder X-ray diffraction (PXRD) using a Bruker D5005 diffractometer employing graphite monochromatised Cu-K$_\alpha$ radiation (λ = 1.54056 Å). Rietveld refinement of the PXRD patterns were performed using TOPAS software. Raman spectra of the samples were recorded on a Renishaw Raman system 2000. Brunauer-Emmett-Teller (BET) surface area studies of the samples were determined from N$_2$ adsorption-desorption isotherms at 77 K using Tristar 3000 (Micromeritics, USA). The samples were preheated for 2 h at 180 °C under nitrogen flow to remove adsorbed moisture prior to BET analysis. Morphology of the samples was examined by scanning electron microscopy (SEM) and Transmission electron Microscopy (TEM). SEM micrographs of the thin layer of platinum coated samples were recorded on a JEOL JSM-6700F field emission scanning electron microscope (FESEM) operated at 5 kV and 10 µA. JEOL JEM 2010 (operated at 200 kV) was used to record the TEM images to determine the surface morphology and the particle size.

Electrochemical properties of the samples were investigated using coin cells (type 2016) with Li metal (Kyokuto Metal Co., Japan) as counter electrode, glass microfiber filter (GF/F,

Whatman Int. Ltd., Maidstone, England) as the separator and 1 M LiPF$_6$ in ethylene carbonate [1] and diethyl carbonate (DEC) (1:1:1 v/v, Merck) as the electrolyte. Firstly, a slurry was prepared by mixing the sample with super P carbon black (15 wt %) and PVDF binder, Kynar 2801 (15 wt %) in N-methyl pyrrolidinone (NMP) solvent. The slurry was stirred for 12 h and then coated onto an etched copper foil, dried at 80 °C and cut into circular discs of 16 mm diameter. Coin cells were assembled in an Ar-filled glove box (MBraun, Germany) with oxygen and water concentration maintained below 1 ppm, by crimp sealing the thus fabricated anode with lithium metal as counter electrode. The cells were aged for 8 h before they were subjected to the electrochemical testing. Cyclic voltammetry and galvanostatic discharge−charge cycling studies of the cells were carried out at room temperature using computer controlled MacPile II (Bio-logic, France) and Bitrode multiple battery tester (model SCN, Bitrode, U.S.A.), respectively. Impedance spectroscopy measurements were carried out in the frequency range of 180 kHz to 0.003 Hz using Solartron 1260A impedance analyzer.

Results and Discussion
Structure and Morphology

During the synthesis, addition of NH$_4$OH to GO/FeSO$_4$ solution gave out an amorphous black powder which was dried at 80 °C to get rGO/Fe$_3$O$_4$ composite. It was also annealed at different conditions as mentioned earlier to study the effect of annealing temperature on the electrochemical properties. Powder X-ray diffraction pattern of the different rGO/Fe$_3$O$_4$ composites are shown in Fig. 1. For each sample, all the diffraction peaks match well with the standard pattern (JCPDS card no: 75-0033) and can be indexed to the cubic space group Fd3m. Fe$_3$O$_4$ exhibits a normal spinel structure containing iron in a mixed-valent (Fe$^{2+/3+}$) state. The divalent Fe^{2+} ions (r_i = 0.74 Å) and the trivalent Fe^{3+} ions (r_i = 0.69 Å) occupy the tetrahedral and octahedral sites respectively. Absence of any impurity peaks such as other iron oxides (Fe$_2$O$_3$ and FeO) indicates the phase purity of the prepared composites. In addition, the absence of GO peaks in the rGO/Fe$_3$O$_4$ composites indicates the reduction of graphene oxide to rGO. The sample prepared at 80 °C shows slightly broadened peaks compared to high temperature annealed samples. This indicates the increase in crystallinity and particle size of Fe$_3$O$_4$ with increase in the annealing temperature. Fig. 2 shows the Rietveld refinement of rGO/Fe$_3$O$_4$. The experimental pattern matches well with the calculated pattern as evidenced from the difference pattern. The lattice parameter (a) of the different composites were obtained from the Rietveld refinement of respective PXRD pattern (Table S1). The lattice parameter of rGO/Fe$_3$O$_4$ obtained at 80 °C in air, 600 °C in Ar, 700 °C in Ar and 700 °C in Ar-H$_2$ are calculated to be 8.3665(1), 8.3700(4), 8.3947(9) and 8.3824(6) Å respectively. The values match well with the reported lattice parameter of Fe$_3$O$_4$.[34]
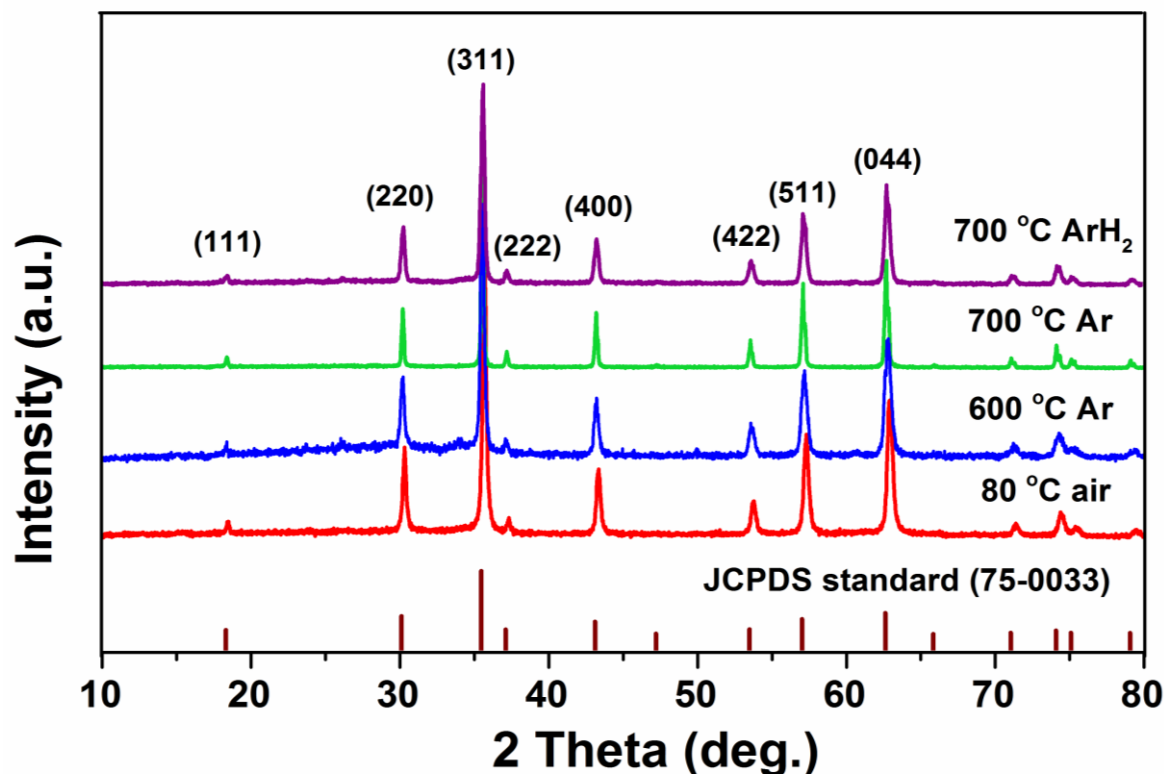
Fig. 1 PXRD patterns of rGO/ Fe$_3$O$_4$ nanocomposites synthesized at different conditions
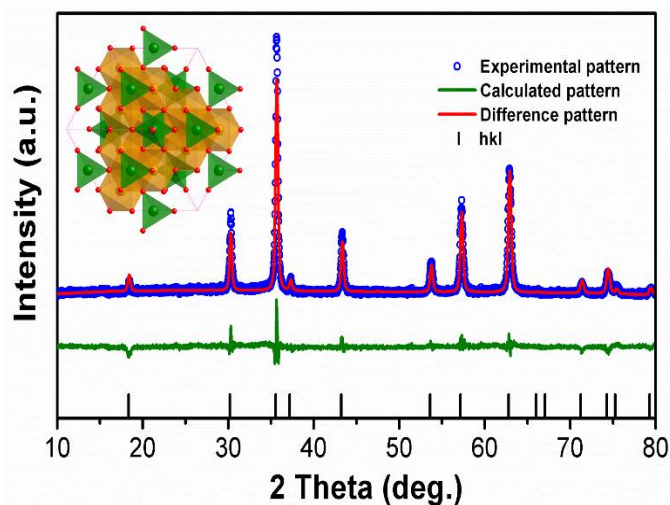
Fig. 2 Rietveld refinement of rGO/Fe$_3$O$_4$ (80 °C in air). Blue circles (○) show the experimental pattern while the red and green lines indicate the calculated pattern and the difference between observed and calculated patterns, respectively.

Raman spectroscopy is an important technique to characterize graphene based materials. Fig. S1 shows the Raman spectra of different rGO/Fe$_3$O$_4$ composites recorded at room temperature in the range of 2000-1000 cm^{-1}. Bare GO shows Raman bands at 1600 and 1350 cm^{-1} which are described as G and D bands respectively. The D band refers to the defects and disordered atomic arrangement due to the sp^3-carbon atom and the vibration of the sp^2-carbon atoms in the two dimensional lattice gives rise to the G band. Upon reduction of graphene oxide to rGO, the intensity ratio of the D band to the G band (I$_D$/I$_G$) increases. In the case of different rGO/Fe$_3$O$_4$ composites, the characteristic G and D bands appear at ~1580 and ~1350 cm^{-1} respectively. The I$_D$/I$_G$ ratio of the composites are greater than 1 except the sample annealed at 700 °C in Ar which shows a ratio slightly lesser than 1. This higher I$_D$/I$_G$ ratio of the rGO/Fe$_3$O$_4$ composites indicates the in-situ reduction of graphene oxide. The G band of the composites shifts by ~20 cm^{-1} which indicates the incorporation of Fe$_3$O$_4$ nanoparticles into the rGO layers.

Morphology and particle size of the different rGO/Fe$_3$O$_4$ nanocomposites were probed using SEM and TEM techniques. Fig. 3 shows the SEM images of the nanocomposites. The sample obtained at 80 °C consists of nanoparticles of size ~20-50 nm wrapped by rGO layers (Fig. 3b). The rGO layers can be seen clearly from the TEM image (Fig. 4a). The presence of rGO along with the Fe$_3$O$_4$ nanoparticles is expected to improve the electronic conductivity compared to bare Fe$_3$O$_4$. With increase in the annealing temperature to 600 °C, the particles form aggregates as seen in Fig. 3d. However, the individual particle size was still ~50-100 nm. With further increase in the annealing temperature to 700 °C in Ar, the particles fuse together to form bigger particles of ~50-200 nm in size. Loss of some rGO content at higher temperature also plays a role in the fusion of individual particles.
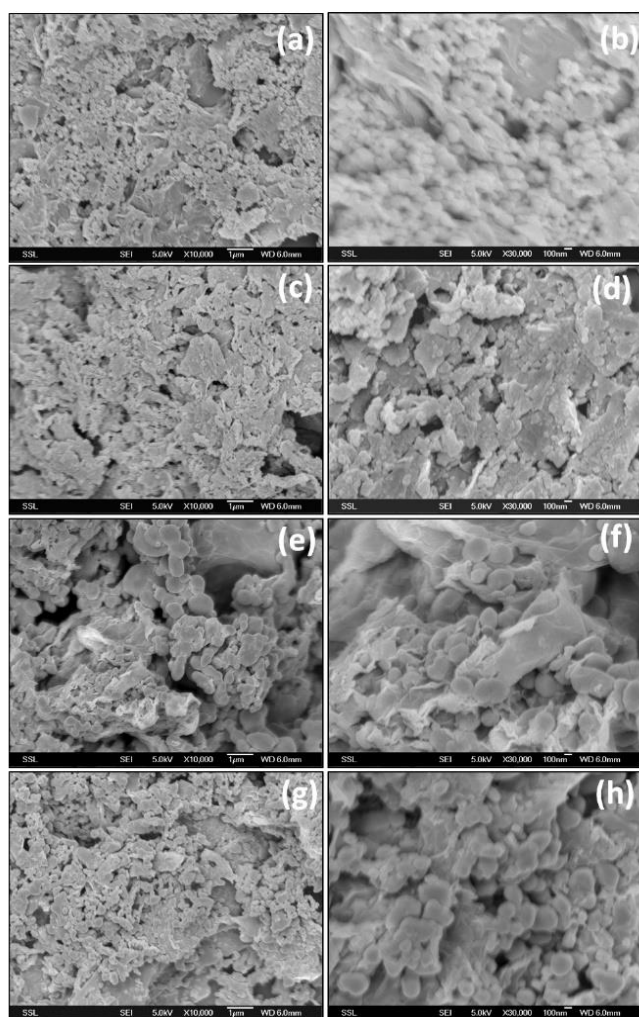
Fig. 3 Scanning Electron micrographs of rGO/ Fe$_3$O$_4$ nanocomposites annealed at (a & b) 80 ºC in air; (c & d) 600 ºC in Ar; (e & f) 700 ºC in Ar and (g & h) 700 ºC in Ar-H$_2$.
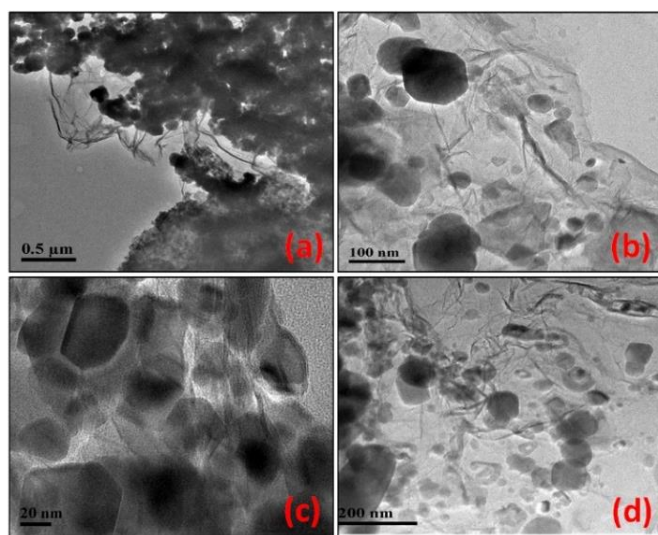
Fig. 4 Transmission Electron micrographs of rGO/Fe$_3$O$_4$ nanocomposites annealed at (a) 80 ºC in air; (b & c) 600 ºC in Ar; (d) 700 ºC in Ar-H$_2$

Nitrogen adsorption-desorption isotherms of the rGO/Fe$_3$O$_4$ composites are shown in Fig. 5. The rGO/Fe$_3$O$_4$ (80 ºC) shows a high BET surface area of 30 m^2 g^{-1} though the amount of rGO in the composite was only 4%. This high surface area can be attributed to the small particle size of Fe$_3$O$_4$ and presence of rGO sheets in the composite. The samples annealed at higher temperatures show decreased surface area due to increase in the particle size, aggregation and slight decrease in the rGO content. The BET surface area, pore size and pore volume of the different rGO/Fe$_3$O$_4$ samples are compared in Table S1.
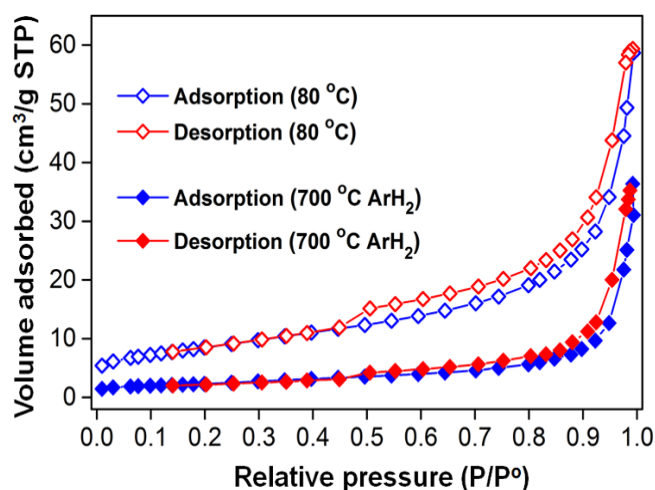
Fig. 5 Nitrogen adsorption-desorption isotherms of rGO/Fe$_3$O$_4$ nanocomposites annealed at 80 ºC in air and 700 ºC in Ar-H$_2$

Galvanostatic cycling

Galvanostatic cycling studies of the different composites were carried out in the potential window, 0.005–3.0 V *vs.* Li/Li$^+$ to investigate the Li-storage and cycleability. A constant current density of 60 mA g^{-1} was used for the testing at room temperature. The charge-discharge profiles of the composites for few selected cycles are shown in Fig. 6a-d.

The first discharge curve of all the rGO/Fe$_3$O$_4$ composites are different from the remaining cycles indicating a different lithium storage mechanism during the initial discharge. It starts from the open circuit voltage (~2.9 V) and shows a steep decrease in the voltage to 1.6 V followed by two small plateaus at ~1.6 and ~1.0 V. These plateaus correspond to the Li-intercalation into Fe$_3$O$_4$ forming a lithium intercalated phase, Li$_x$Fe$_3$O$_4$ (x ≈ 2) as shown in eq. 1. During this reaction, the two Fe^{3+} ions in Fe$_3$O$_4$ are reduced to Fe^{2+}. Except for the sample prepared at 700 ºC in Ar, this plateau was observed in all the composites. Further decrease in the voltage results in lithiation of the intercalated phase as indicated by a large plateau at ~0.85 V. During this process, 6 more moles of Li are consumed as per eq. 2, resulting in an irreversible destruction of the crystal structure. This process is accompanied by the reduction of all Fe^{2+} ions to Fe metal nanoparticles which are embedded in an amorphous Li$_2$O matrix.[35] Thus 8 moles of Li are utilized per mole of Fe$_3$O$_4$, corresponding to a theoretical capacity of 926 mAh g^{-1}. However, the first discharge capacities observed for rGO/Fe$_3$O$_4$

obtained at 80 °C (air), 600 °C (Ar), 700 °C (Ar) and 700 °C (Ar-H$_2$) were 1855, 1716, 1406 and 1554 mAh g^{-1} respectively. This additional capacity can be explained as the formation of solid electrolyte interface (SEI) by the reaction of lithium with the solvents of the electrolyte.[24, 36] In addition, rGO present in the samples (3-4 %) also contributes to lithium storage and SEI formation.[30]

During the first charge cycle, Lithium is extracted from the material at ~1.4-2.0 V as indicated by a slopping plateau. The Li$_2$O and Fe nanoparticles formed during the initial discharge cycle react with each other to form iron oxide according to eq. 3. The first charge capacities obtained for rGO/Fe$_3$O$_4$ synthesized at 80 °C in air, 600 °C in Ar, 700 °C in Ar and 700 °C in Ar-H$_2$ were 1254, 1082, 853 and 1001 mAh g^{-1} respectively. The second discharge curve in all the samples are different from the first discharge cycle. The second and subsequent cycles rely on the reversible conversion of iron oxide to Fe nanoparticles embedded in Li$_2$O matrix. The voltage of the discharge plateau also shifts to ~1.0 V compared to 0.85 V observed for the first cycle.

$$Fe_3O_4 + x\ Li^+ + x\ e^- \rightarrow Li_xFe_3O_4 \dots\dots\dots\dots\dots\dots\dots(1)$$
$$Li_xFe_3O_4 + (8-x)\ Li^+ + (8-x)\ e^- \rightarrow 3\ Fe + 4\ Li_2O \dots\dots(2)$$
$$3\ Fe + 4\ Li_2O \leftrightarrow Fe_3O_4 + 8\ Li^+ + 8\ e^- \dots\dots\dots\dots\dots..(3)$$
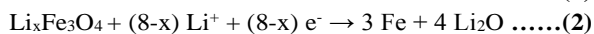
The conversion reaction happening in the rGO/Fe$_3$O$_4$ anodes is found to be highly reversible as inferred from the overlapping charge-discharge curves of the different cycles (Fig. 7). The variation of charge and discharge capacities with cycle number of the different composites and their corresponding coulombic efficiencies are shown in Fig. 7. The sample obtained at 80 °C shows the highest charge capacity of 1254 mAh g^{-1} for the first cycle which can be attributed to smaller particle size and high surface area. However, the cycling stability was slightly poor resulting in a capacity of 1046 mAh g^{-1} at the end of 40 cycles which is still higher than the theoretical capacity. Upon increase in the annealing temperature, the particle size of Fe$_3$O$_4$ increases and hence the surface area decreases dramatically. The sample obtained at 600 °C in Ar shows a slightly lesser capacity 1082 mAh g^{-1} for the first cycle. However, it exhibits better cycling stability with a capacity of 1062 mAh g^{-1} obtained at the end of 40 cycles.

With further increase in annealing temperature to 700 °C, the capacity decreases further due to slightly decreased graphene content and increased particle size. The charge capacity obtained for the samples annealed at 700 °C in Ar and Ar-H$_2$ environment were 853 and 1001 mAh g^{-1}. However, capacity retention of these samples were found to be excellent with reversible capacity of 854 and 972 mAh g^{-1} obtained after 40 cycles. In addition, all the composites possess high coulombic efficiency of ~99 %. The details of the charge and discharge capacities of the individual samples for the 1st, 2nd and 40th cycles are listed in Table 1. Though the reversible capacities obtained for these composites are quite high and stable, high polarization of ~ 0.6 V is observed which is characteristic of these oxides. Though many reports on

rGO/Fe$_3$O$_4$ appear in the literature, the graphene/rGO content in the samples were very high leading to good capacity.[37-40] In this study, better electrochemical performance was achieved for the rGO/Fe$_3$O$_4$ samples, though the rGO content was only 3-4 %.
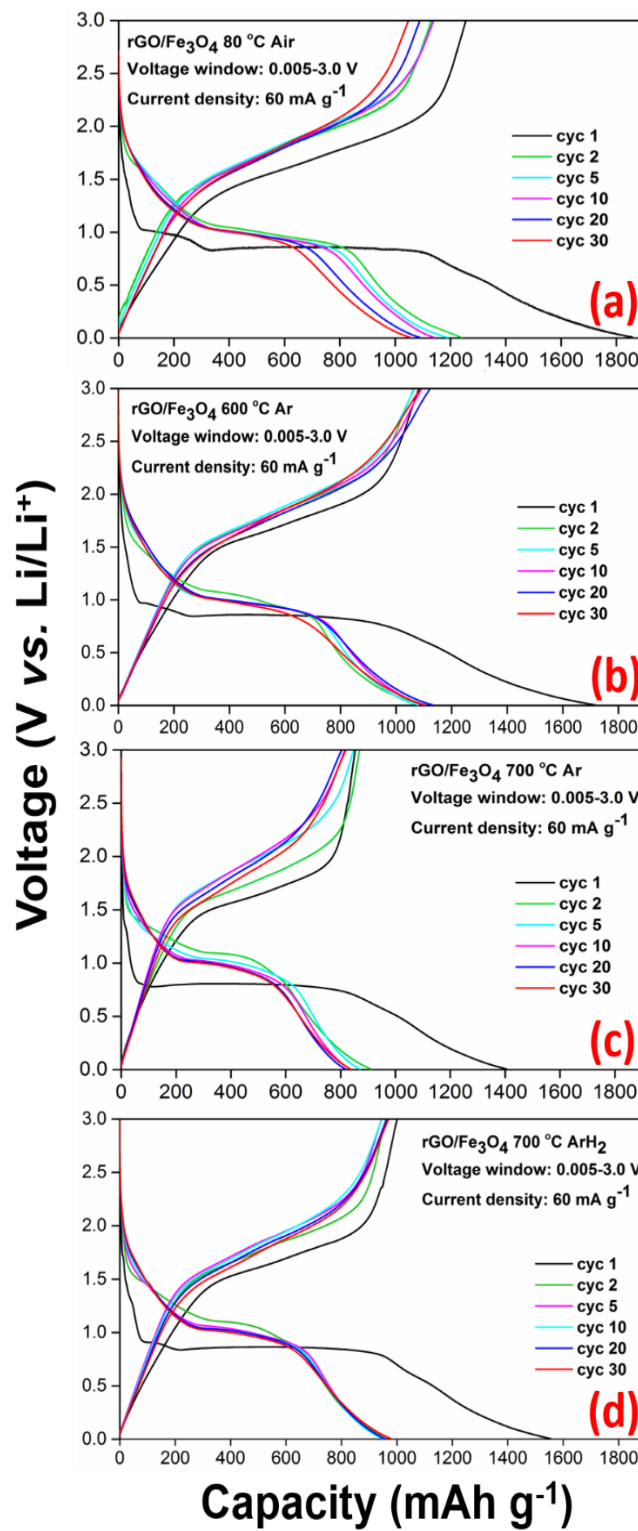
Fig. 6 Galvanostatic cycling studies showing charge-discharge profiles of rGO/Fe$_3$O$_4$ synthesized at (a) 80 °C in air; (b) 600 °C in Ar; (c) 700 °C in Ar and (d) 700 °C in Ar-H$_2$.
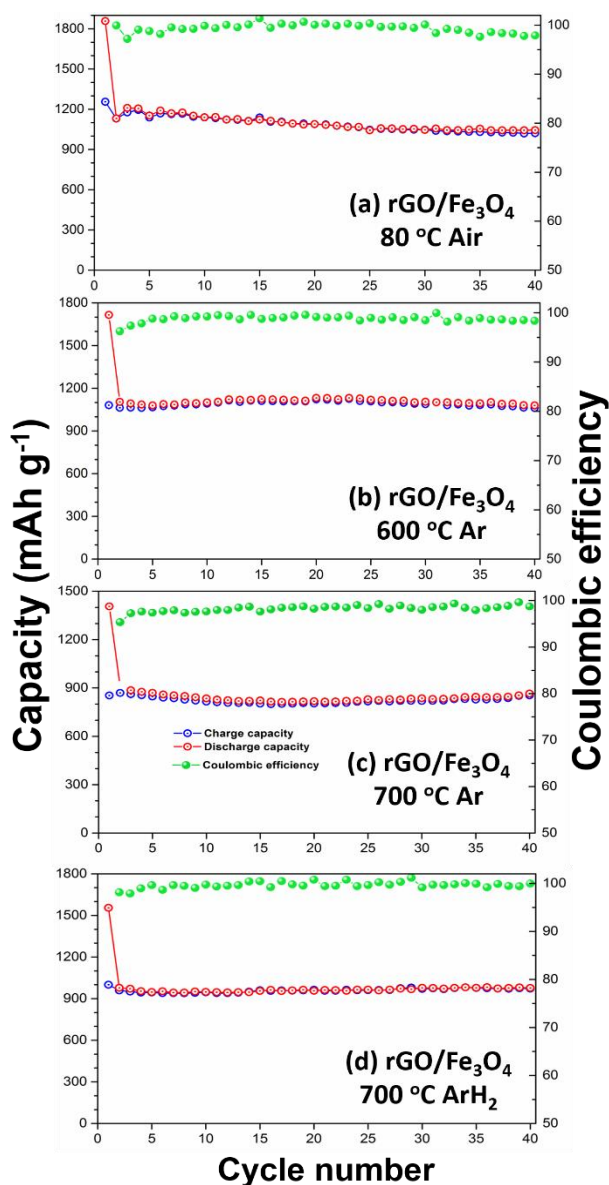
Fig. 7 Capacity *vs.* cycle number plots of rGO/Fe$_3$O$_4$ nanocomposites synthesized at (a) 80 ºC in air; (b) 600 ºC in Ar; (c) 700 ºC in Ar and (d) 700 ºC in Ar-H$_2$.

Table 1. Charge and discharge capacities of rGO/Fe$_3$O$_4$ nanocomposites synthesized at different conditions

Compound	Discharge capacity (mAh g^{-1})			Charge capacity (mAh g^{-1})		
	1st cycle	2nd cycle	40th cycle	1st cycle	2nd cycle	40th cycle
rGO/Fe$_3$O$_4$ 80 ºC in air	1855	1236	1047	1254	1127	1046
rGO/Fe$_3$O$_4$ 600 ºC in Ar	1716	1105	1080	1082	1063	1062
rGO/Fe$_3$O$_4$ 700 ºC in Ar	1406	911	865	853	869	854
rGO/Fe$_3$O$_4$ 700 ºC in ArH$_2$	1554	978	977	1001	960	972

Rate capability studies

High rate capability is an important characteristic of a good electrode material. Rate capability studies help in understanding the ability of the material to store lithium at different current rates. A material with a good capacity at high current rates is very useful as it can be charged and discharged in a short time. All the different rGO/Fe$_3$O$_4$ composites were subjected to galvanostatic charge-discharge cycling at different current densities of 500, 1000, 2000 and 3000 mA g^{-1} which corresponds to the current rates of ~0.5, 1.1, 2.2 and 3.2 C respectively (1 C represents a current density of 926 mA g^{-1}). As expected, specific capacity of the composites decreases when the current density was increased from 60 mA g^{-1} to higher current densities. Fig. 8 shows the capacity *vs.* cycle number plots at different current rates for the rGO/Fe$_3$O$_4$ composites synthesized at different conditions. The sample obtained at 600 ºC in Ar shows the best performance at 500 and 1000 mA g^{-1}. However, at higher rates, the reversible capacity obtained was poor. The sample annealed at 700 ºC in Ar-H$_2$ shows the best capacity retention at high current rates. This can be attributed to the better reduction of rGO in a reducing Ar-H$_2$ environment. When the current was decreased from 3000 to 60 mA g^{-1}, the capacity obtained was found to be higher than the original capacity obtained at 60 mAg^{-1}. This increase in capacity can be attributed to the increase in the activity of graphene upon cycling, as evidenced by the large capacity obtained after the plateau region (Fig. S2).
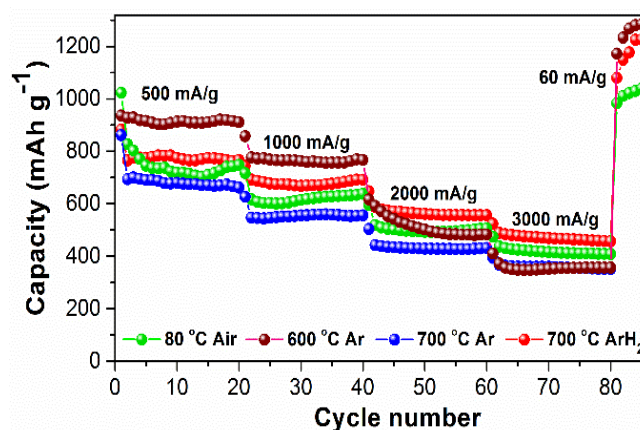
Fig. 8 Rate capability of rGO/Fe$_3$O$_4$ nanocomposites synthesized at different conditions

Cyclic voltammetry

Cyclic voltammetry (CV) is a complementary technique to galvanostatic cycling which gives information about the redox potentials of electrochemical reactions occurring in the electrodes. Fig. 9 shows the cyclic voltammograms of the different rGO/Fe$_3$O$_4$ composites for selected cycles. The experiments were carried out at room temperature using Li metal as the counter electrode in the potential window of 0.005−3 V at a constant scan rate of 58 µV s$^{−1}$. All the four samples show similar CV curves and their first cycle exhibits substantial difference with the subsequent cycles. During the first cathodic scan (reduction or Li-insertion), two small peaks at ~1.4 and ~0.8

V were observed which are due to the formation of a lithium intercalated compound $Li_xFe_3O_4$ from the magnetite phase (Fe_3O_4) as per eq. 1.
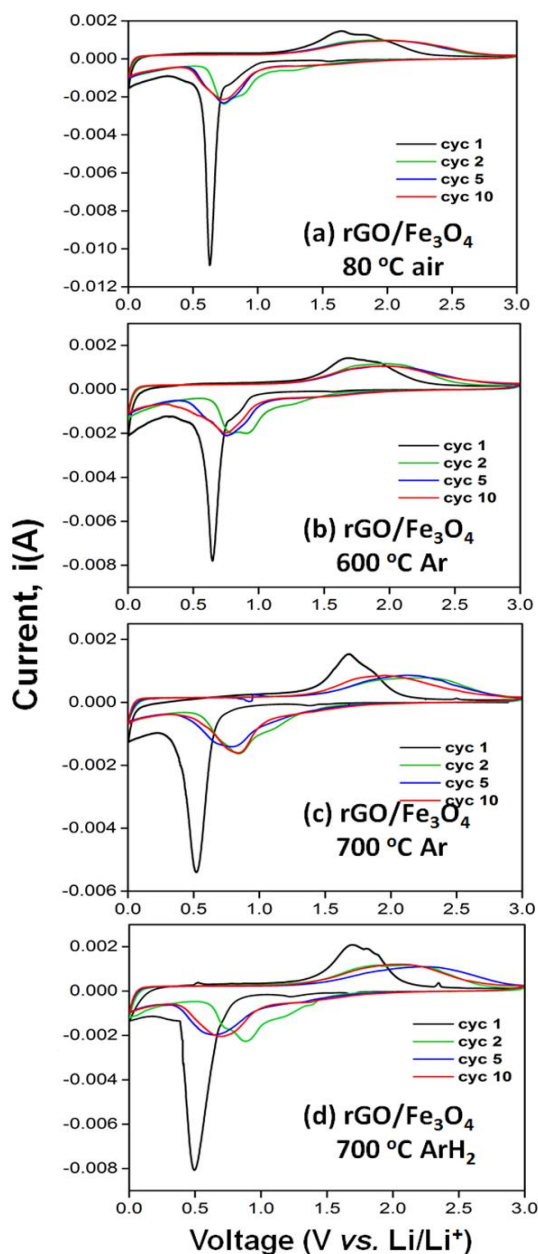
Fig.9 Cyclic voltammograms (CV) of rGO/Fe_3O_4 synthesized at (a) 80 °C in air; (b) 600 °C in Ar; (c) 700 °C in Ar and (d) 700 °C in Ar-H_2.

In the case of sample annealed at 700 °C in Ar, the peak at 0.8 V did not appear, similar to the galvanostatic cycling results. Upon further discharge to the cut-off voltage of 0.005 V, a sharp peak appears at ~0.5-0.6 V, which corresponds to crystal structure destruction of Fe_3O_4 forming Fe nanoparticles embedded in Li_2O matrix. This peak was not seen in the subsequent cycles, indicating the irreversible nature of the first discharge cycle (eq. 2). The first anodic scan shows two overlapped peaks at ~1.7 V which correspond to the oxidation of

Fe to form Fe_3O_4 (eq. 3). In the subsequent cycles, a single broad peak was observed at 0.7-0.8 V for the different composites during cathodic scans and 2.0 V during the anodic scans. Similar redox potentials have been reported for magnetite anode materials. The overlapping CV curves also indicate excellent reversibility of lithium cycling in the material.

Electrochemical Impedance Spectroscopy

EIS is an important technique used to analyse electrode kinetics. The impedance measurements were carried out for the different rGO/Fe_3O_4 nanocomposites for the 1st and 40th cycles at selected voltages. During voltage increment (charging) and decrement (discharging), the cell was subjected to a current density of ~200 mA g^{-1} and was relaxed at the given voltage for 2h before data collection. The results are plotted as Nyquist plots (Z_{re} vs. Z_{im}), where Z_{re} and Z_{im} are respectively the real and imaginary parts of cell impedance.

Fig. S3a compares the Nyquist plots obtained at open circuit voltage for all the different composites. They showed a single semicircle with an overall impedance of ~220-250 Ω except for the 80 °C sample which shows only 120 Ω. This large semicircle is attributed mainly to the high surface film resistance R_{sf} and the associated capacitance, CPE_{sf}. With the onset of lithium insertion, the surface film resistance is expected to decrease and the charge transfer resistance increases. The overall impedance has been observed to be ~60-80 Ω at the fully discharged state (0.005 V) as shown in Figure S3b where the Fe_3O_4 particles are disintegrated to Fe metal nanoparticles in Li_2O matrix.

Detailed EIS measurements were carried out for the rGO/Fe_3O_4 composite prepared at 700 °C in Ar-H_2. EIS data were collected for the sample at different voltages for the 1st charge and discharge cycle as shown in Fig. 10. During the discharge cycle, the impedance decreases with the commencement of lithiation and reaches ~70 Ω at the fully discharged state. During the charge cycle, the impedance was very low (15-20 Ω) in the plateau region indicating good conductivity of the sample.

The composites were also subjected to 40 charge-discharge cycles and the EIS data were recorded at the discharged state (Fig. S3c). As can be seen the impedance was very low ~20 Ω for all the samples except the sample annealed at 600 °C in Ar. This explains the good cycling stability of the composites. The fast capacity fading of the sample prepared at 600 °C in Ar can be explained by its high impedance compared to other samples.
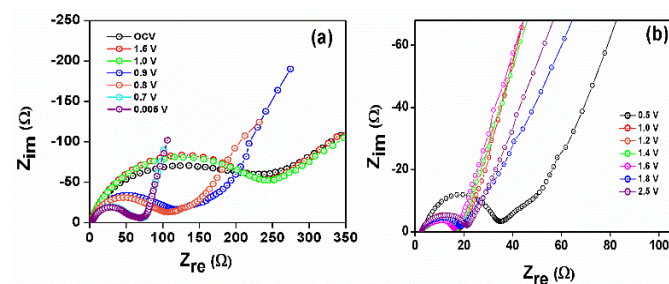
Fig. 10 Nyquist plots of rGO/Fe_3O_4 (700 °C Ar-H_2) at different voltages for (a) 1st discharge and (b) 1st charge cycle

Conclusions

In summary, porous rGO wrapped magnetite nanoparticles were obtained by a simple precipitation reaction followed by freeze drying and heating at 80 °C in air. The sample with ~4% rGO has high surface area of 30 m^2 g^{-1} and exhibits high reversible capacity of over 1200 mAh g^{-1} at a current density of 60 mA g^{-1}. However, the capacity retention was slightly poor. Annealing the composites at higher temperatures leads to increased particle size and decreased surface area. However, these composites exhibits very good lithium cycling properties and minimal capacity fading. The sample annealed at 700 °C in Ar-H$_2$ atmosphere exhibits the best rate capability with a capacity of ~ 480 mAh g^{-1} at a high current rate of 3.2 C (3000 mA g^{-1}).

Notes

ᵃDepartment of Chemistry, National University of Singapore, Singapore 117543. Fax: (+) 65-6779-1691; E-mail: chmjjv@nus.edu.sg
ᵇAdvanced batteries lab, Department of Physics, National University of Singapore, Singapore 117542. Fax: (+) 65-6777-6126; E-mail: phymvvr@nus.edu.sg
ᶜDepartment of Materials Science and Engineering, National University of Singapore, Singapore

References

1. M. V. Reddy, T. Yu, C.-H. Sow, Z. X. Shen, C. T. Lim, G. V. S. Rao and B. V. R. Chowdari, *Adv. Funct. Mater.*, 2007, **17**, 2792-2799.
2. L. Zhang, H. B. Wu and X. W. Lou, *Adv. Energy Mater.*, 2014, **4**, 1300958/1300951-1300958/1300911.
3. X. Zhu, Y. Zhu, S. Murali, M. D. Stoller and R. S. Ruoff, *ACS Nano*, 2011, **5**, 3333-3338.
4. D. Larcher, C. Masquelier, D. Bonnin, Y. Chabre, V. Masson, J.-B. Leriche and J.-M. Tarascon, *J. Electrochem. Soc.*, 2003, **150**, A133-A139.
5. S.-D. Seo, D.-H. Lee, H.-W. Shim, S. Lee and D.-W. Kim, *J. Am. Ceram. Soc.*, 2014, **97**, 1413-1420.
6. P. L. Taberna, S. Mitra, P. Poizot, P. Simon and J. M. Tarascon, *Nat. Mater.*, 2006, **5**, 567-573.
7. G. Zhou, D.-W. Wang, F. Li, L. Zhang, N. Li, Z.-S. Wu, L. Wen, G. Q. Lu and H.-M. Cheng, *Chem. Mater.*, 2010, **22**, 5306-5313.
8. Q.-q. Xiong, J.-p. Tu, Y. Lu, J. Chen, Y.-x. Yu, X.-l. Wang and C.-d. Gu, *J. Mater. Chem.*, 2012, **22**, 18639-18645.
9. A. S. Hameed, H. Bahiraei, M. V. Reddy, M. Z. Shoushtari, J. J. Vittal, C. K. Ong and B. V. R. Chowdari, *ACS Appl. Mater. Interfaces*, 2014, **6**, 10744-10753.
10. Y. Sharma, N. Sharma, G. V. S. Rao and B. V. R. Chowdari, *Electrochim. Acta*, 2008, **53**, 2380-2385.
11. H. Tang, P. Gao, A. Xing, S. Tian and Z. Bao, *RSC Adv.*, 2014, **4**, 28421-28425.
12. C. T. Cherian, J. Sundaramurthy, M. V. Reddy, P. Suresh Kumar, K. Mani, D. Pliszka, C. H. Sow, S. Ramakrishna and B. V. R. Chowdari, *ACS Appl. Mater. Interfaces*, 2013, **5**, 9957-9963.
13. P. Lavela and J. L. Tirado, *J. Power Sources*, 2007, **172**, 379-387.
14. N. Wang, H. Xu, L. Chen, X. Gu, J. Yang and Y. Qian, *J. Power Sources*, 2014, **247**, 163-169.
15. M. V. Reddy, G. V. Subba Rao and B. V. R. Chowdari, *Chemical Reviews*, 2013, **113**, 5364-5457.
16. F. Jiao, J. Bao and P. G. Bruce, *Electrochem. Solid-State Lett.*, 2007, **10**, A264-A266.
17. Y. Chen, B. Song, X. Tang, L. Lu and J. Xue, *J. Mater. Chem.*, 2012, **22**, 17656-17662.
18. C. Wang, G. Shao, Z. Ma, S. Liu, W. Song and J. Song, *Electrochim. Acta*, 2014, **130**, 679-688.
19. C. Ban, Z. Wu, D. T. Gillaspie, L. Chen, Y. Yan, J. L. Blackburn and A. C. Dillon, *Adv. Mater.*, 2010, **22**, E145-E149.
20. J.-Z. Wang, C. Zhong, D. Wexler, N. H. Idris, Z.-X. Wang, L.-Q. Chen and H.-K. Liu, *Chem. - Eur. J.*, 2011, **17**, 661-667.
21. P. Wang, M. Gao, H. Pan, J. Zhang, C. Liang, J. Wang, P. Zhou and Y. Liu, *J. Power Sources*, 2013, **239**, 466-474.
22. P. Lv, H. Zhao, Z. Zeng, J. Wang, T. Zhang and X. Li, *J. Power Sources*, 2014, **259**, 92-97.
23. L. Lang and Z. Xu, *ACS Appl. Mater. Interfaces*, 2013, **5**, 1698-1703.
24. W.-M. Zhang, X.-L. Wu, J.-S. Hu, Y.-G. Guo and L.-J. Wan, *Adv. Funct. Mater.*, 2008, **18**, 3941-3946.
25. T. Zhu, J. S. Chen and X. W. Lou, *J. Phys. Chem. C*, 2011, **115**, 9814-9820.
26. B. Wang, G. Wang, Z. Zheng, H. Wang, J. Bai and J. Bai, *Electrochimica Acta*, 2013, **106**, 235-243.
27. J. Cheng, B. Wang, C.-M. Park, Y. Wu, H. Huang and F. Nie, *Chem. - Eur. J.*, 2013, **19**, 9866-9874.
28. Y. Wu, Y. Wei, J. Wang, K. Jiang and S. Fan, *Nano Lett*, 2013, **13**, 818-823.
29. Y. Liu, K. Huang, H. Luo, H. Li, X. Qi and J. Zhong, *RSC Adv.*, 2014, **4**, 17653-17659.
30. T.-q. Wang, X.-l. Wang, Y. Lu, Q.-q. Xiong, X.-y. Zhao, J.-b. Cai, S. Huang, C.-d. Gu and J.-p. Tu, *RSC Adv.*, 2014, **4**, 322-330.
31. C. Wang, Q. Zhang, Q.-H. Wu, T.-W. Ng, T. Wong, J. Ren, Z. Shi, C.-S. Lee, S.-T. Lee and W. Zhang, *RSC Adv.*, 2012, **2**, 10680-10688.
32. W. S. Hummers, Jr. and R. E. Offeman, *J. Am. Chem. Soc.*, 1958, **80**, 1339.
33. N. I. Kovtyukhova, P. J. Ollivier, B. R. Martin, T. E. Mallouk, S. A. Chizhik, E. V. Buzaneva and A. D. Gorchinskiy, *Chem. Mater.*, 1999, **11**, 771-778.
34. B. Bateer, C. Tian, Y. Qu, S. Du, T. Tan, R. Wang, G. Tian and H. Fu, *CrystEngComm*, 2013, **15**, 3366-3371.
35. S. Bhuvaneswari, P. M. Pratheeksha, S. Anandan, D. Rangappa, R. Gopalan and T. N. Rao, *Phy. Chem. Chem. Phy.*, 2014, **16**, 5284-5294.
36. C. T. Cherian, J. Sundaramurthy, M. Kalaivani, P. Ragupathy, P. S. Kumar, V. Thavasi, M. V. Reddy, C. H. Sow, S. G. Mhaisalkar, S. Ramakrishna and B. V. R. Chowdari, *J. Mater. Chem.*, 2012, **22**, 12198-12204.
37. P. Lian, X. Zhu, H. Xiang, Z. Li, W. Yang and H. Wang, *Electrochimica Acta*, 2010, **56**, 834-840.
38. R. Wang, C. Xu, J. Sun, L. Gao and C. Lin, *Journal of Materials Chemistry A*, 2013, **1**, 1794-1800.
39. J. Su, M. Cao, L. Ren and C. Hu, *J. Phys. Chem. C*, 2011, **115**, 14469-14477.
40. C. Liang, T. Zhai, W. Wang, J. Chen, W. Zhao, X. Lu and Y. Tong, *J. Mater. Chem. A*, 2014, **2**, 7214-7220.

RSC Advances Accepted Manuscript

TOC graphic
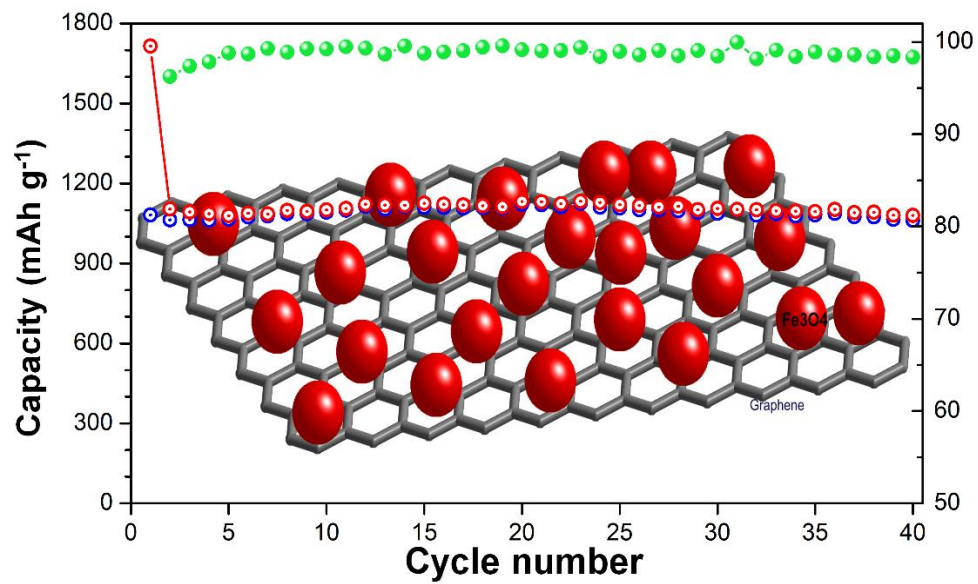
RGO wrapped magnetite nanocomposites obtained by a simple precipitation and freeze drying exhibiting stable and high reversible lithium storage